3. E. Seidemann, W. T. Newsome, *J. Neurophysiol.* **81**, 1783 (1999).
4. C. L. Colby, M. E. Goldberg, *Annu. Rev. Neurosci.* **22**, 319 (1999).
5. S. Treue, J. H. R. Maunsell, *J. Neurosci.* **19**, 7591 (1999).
6. R. A. Andersen, C. A. Buneo, *Annu. Rev. Neurosci.* **25**, 189 (2002).
7. R. Desimone, J. Duncan, *Annu. Rev. Neurosci.* **18**, 193 (1995).
8. J. M. Wolfe, K. R. Cave, S. L. Franzel, *J. Exp. Psychol. Hum. Percept. Perform.* **15**, 419 (1989).
9. L. Chelazzi, E. K. Miller, J. Duncan, R. Desimone, *Cereb. Cortex* **11**, 761 (2001).
10. J. A. Mazer, J. L. Gallant, *Neuron* **40**, 1241 (2003).
11. T. Ogawa, H. Komatsu, *J. Neurosci.* **24**, 6371 (2004).
12. P. E. Haenny, J. H. Maunsell, P. H. Schiller, *Exp. Brain Res.* **69**, 245 (1988).
13. B. C. Motter, *J. Neurosci.* **14**, 2178 (1994).
14. C. J. McAdams, J. H. R. Maunsell, *J. Neurophysiol.* **83**, 1751 (2000).
15. P. Fries, P. R. Roelfsema, A. K. Engel, P. Konig, W. Singer, *Proc. Natl. Acad. Sci. U.S.A.* **94**, 12699 (1997).
16. M. R. Jarvis, P. P. Mitra, *Neural Comput.* **13**, 717 (2001).
17. P. Fries, J. H. Reynolds, A. E. Rorie, R. Desimone, *Science* **291**, 1560 (2001).
18. B. Pesaran, J. S. Pezaris, M. Sahani, P. P. Mitra, R. A. Andersen, *Nat. Neurosci.* **5**, 805 (2002).
19. E. Salinas, T. J. Sejnowski, *J. Neurosci.* **20**, 6193 (2000).
20. Materials and methods are available as supporting material on *Science* Online.
21. Several lines of evidence suggest that the monkeys used the feature of the cue to guide their search and did not make fixations around the array randomly. First, we did not find any evidence for regular scan patterns, and the average number of saccades to find the target under the different conditions was always significantly less than the number of saccades that would be required to find the target by chance (fig. S2A) (*t* tests, $P < 10^{-5}$). Second, the median fixation duration across those saccades was less than half and

significantly less than the minimum 700-ms fixation duration required to correctly signal the acquisition of the target (fig. S2A) ($P < 10^{-5}$). Finally, the pattern of fixations on distracters indicated that the target color had a large effect on the distracters that were fixated. During color search, monkeys were significantly more likely to fixate a distracter with a color similar to the cued target color (e.g., an orange or magenta stimulus if the cue was red) or distracters with the second cued color in a given session than they were to fixate other distracters (fig. S2B) (analysis of variance, $P < 10^{-5}$; group comparisons, $P < 0.05$). Likewise, they also fixated distracters with colors similar to the cued color significantly longer than other distracters (fig. S2B) (analysis of variance, $P < 10^{-5}$; group comparisons, $P < 0.05$). For shape search, there was no reliable method to measure perceptual similarity among shapes. However, consistent with the results in color search, the monkeys showed significant differences in fixations on distracters depending on the shape of the searched-for target.
22. Across the population, there were no significant differences in either the average fixation number or the relative contribution of the first fixation after array onset to the data used in comparing the four conditions of interest for each visual search.
23. Fifteen sessions were performed with one monkey and twelve with the other.
24. Forty-four neurons (in 23 sessions) contributed to the analysis of feature enhancement during color search based on significant color selectivity for the two color cues used, and 38 neurons (in 21 sessions) contributed to the analysis of feature enhancement during shape search based on significant shape selectivity. Sixty-one and 57 LFP signals contributed to the analyses of color and shape search, respectively.
25. We calculated the coherence between spikes on one electrode and the LFP recorded on all other electrodes separately. It made no difference in the overall results whether the LFP from the same electrode was used or not, and therefore we included it in our analyses.

26. Of these neurons, 15 contributed to the analysis of color enhancement and 16 to the analysis of shape enhancement.
27. N. P. Bichot, J. D. Schall, *Nat. Neurosci.* **2**, 549 (1999).
28. Fixation probability was greater and fixation duration increased for distracters that shared one of the cue features, although there was a clear bias in favor of selecting stimuli that matched the color of the target compared to stimuli matching the shape (fig. S2B) (analysis of variance, $P < 10^{-5}$; group comparisons, $P < 0.05$).
29. Using the conjunction search data, we found that the lack of saccadic enhancement in the spike-field coherence was not dependent on the properties of the RF stimulus.
30. E. A. Buffalo, R. Desimone, unpublished data.
31. J. H. Reynolds, L. Chelazzi, R. Desimone, *J. Neurosci.* **19**, 1736 (1999).
32. J. Moran, R. Desimone, *Science* **229**, 782 (1985).
33. K. R. Cave, M. S. Kim, N. P. Bichot, K. V. Sobel, in *Neurobiology of Attention*, L. Itti, G. Rees, J. Tsotsos, Eds. (Elsevier, Boston, 2004), pp. 547–552.
34. E. K. Miller, C. A. Erickson, R. Desimone, *J. Neurosci.* **16**, 5154 (1996).
35. K. G. Thompson, N. P. Bichot, *Prog. Brain Res.* **147**, 251 (2005).
36. F. H. Hamker, *Cereb. Cortex* **15**, 431 (2005).
37. We thank Plexon, Inc., for technical assistance, and P. Fries, P. Mitra, K. Thompson, and J. Schall for valuable comments. Supported by the NIMH Intramural Research Program.

REPORTS

Sub–Diffraction-Limited Optical Imaging with a Silver Superlens

Nicholas Fang, Hyesog Lee, Cheng Sun, Xiang Zhang*

Recent theory has predicted a superlens that is capable of producing sub–diffraction-limited images. This superlens would allow the recovery of evanescent waves in an image via the excitation of surface plasmons. Using silver as a natural optical superlens, we demonstrated sub–diffraction-limited imaging with 60-nanometer half-pitch resolution, or one-sixth of the illumination wavelength. By proper design of the working wavelength and the thickness of silver that allows access to a broad spectrum of subwavelength features, we also showed that arbitrary nanostructures can be imaged with good fidelity. The optical superlens promises exciting avenues to nanoscale optical imaging and ultrasmall optoelectronic devices.

Conventional optics suffer from the so-called diffraction limit, because they are only capable of transmitting the propagating components

emanating from the source (*1*). This is because the evanescent waves that carry subwavelength information about the object decay exponentially in a medium with positive permittivity and permeability and are lost before reaching the image plane. To avoid this evanescent decay, a concept of subwavelength imaging through an intimate-contact mask was proposed back in the 1970s (*2*) and was sub-

sequently demonstrated (*3*). Conventional immersion lenses that improve image resolution by increasing the index of refraction are limited by the availability of high-index materials. Although scanning near-field optical microscopy detects subwavelength details, it uses point-by-point scanning rather than forming the whole image at once. Interference can also form simple subwavelength patterns (*4*, *5*), but it is not considered to be an imaging method because of the lack of a general bijective conformal mapping between the object and the image.

In contrast, a superlens is predicted to substantially enhance evanescent waves (*1*), compensating for the evanescent loss outside the superlens and thus restoring an image below the diffraction limit. This unusual lens takes the form of a thin slab of material with negative permittivity or permeability, or both (*1*, *6–10*). Metamaterials (*6–15*), an emerging class of artificially designed and structured materials, have shown unprecedented electromagnetic properties in microwave or terahertz regimes, which provide a basis for the conjecture of the superlens. Although metamaterials and photonic crystals have recently shown beam bending (*8*, *13*, *14*) and refocus-

5130 Etcheverry Hall, Nanoscale Science and Engineering Center, University of California, Berkeley, CA 94720–1740, USA.

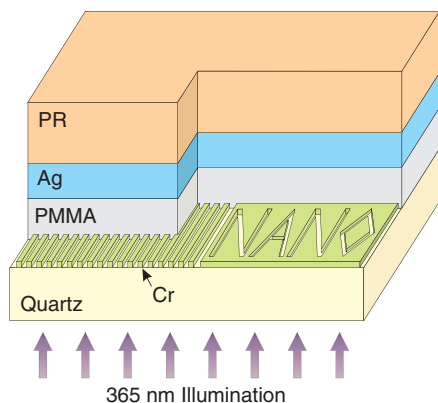*To whom correspondence should be addressed. E-mail: xiang@berkeley.edu

Fig. 1. Optical superlensing experiment. The embedded objects are inscribed onto the 50-nm-thick chrome (Cr); at left is an array of 60-nm-wide slots of 120 nm pitch, separated from the 35-nm-thick silver film by a 40-nm PMMA spacer layer. The image of the object is recorded by the photoresist on the other side of the silver superlens.

Fig. 2. (**A**) AFM of the developed image (scale bar, 1 μm; color scale from dark red to bright yellow, 0 to 150 nm). (**B**) Control experiments were carried out, in which the silver superlens layer was replaced by a 35-nm-thick PMMA layer, for a total PMMA thickness of 75 nm. (**C**) The blue solid curve shows the averaged cross-sectional profile of Fig. 2A, clearly demonstrating the 63 ± 4 nm half-pitch resolved with a 35-nm silver superlens. X, relative displacement along the cross-section direction. (**D**) The blue solid curve shows the average cross section of Fig. 2B (control sample). (**E**) The red and black solid curves show the corresponding surface roughness profile on silver and the PMMA layer above the grating object, respectively.

ing (6, 7, 9, 10, 16) at microwave frequencies, achieving superlensing at optical frequencies is challenging partly because of the diminishing magnetic susceptibility of natural materials. Only recently have metamaterials shown magnetic responses in terahertz and infrared regimes (11, 12). However, in the near field, the electric and magnetic responses of materials are decoupled; therefore, for transverse magnetic (TM) waves, only the permittivity needs to be considered (1). This makes noble metals such as silver natural candidates for optical superlensing, because negative permittivity is easily attainable in them as a consequence of the collective excitation of conduction electrons. Let us consider a superlens consisting of a silver slab separated from an object by a spacer layer, and coated on the opposite side with an imaging material. By designing the thin metal slab so that the surface current oscillations (the surface plasmons) match the evanescent waves from the object, the superlens is able to substantially enhance the amplitude of the field. This key precursor for superlensing—the enhancement of evanescent waves by surface plasmons—was observed on silver films (17). Recently, numerical simulations have been conducted to understand the details of the silver superlens (18–22). However, experimental attempts reported diffraction-limited images, probably resulting from the use of thick silver films that hinder the enhancement of evanescent waves (20).

As surface charges accumulate at the interface between the silver and the imaging medium, the normal component of an electric field is found at resonance when a proper thickness of silver is selected and the permittivity of the silver and that of the adjacent medium are equal and of opposite sign. Such a delicate resonance is essential to ensure the evanescent enhancement across the slab (1, 22).
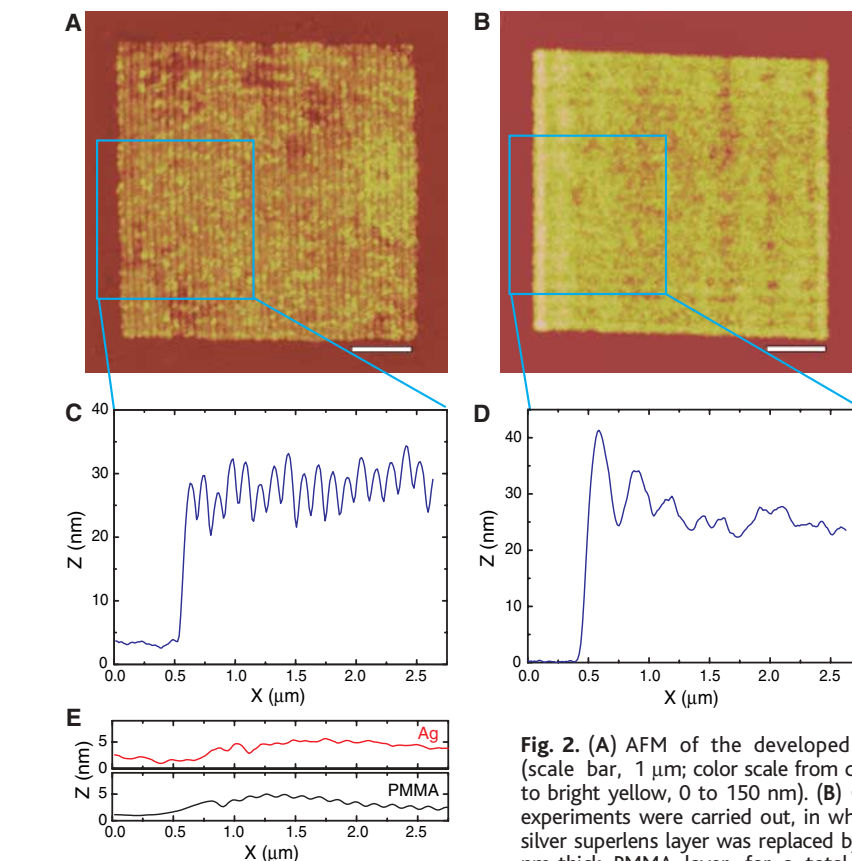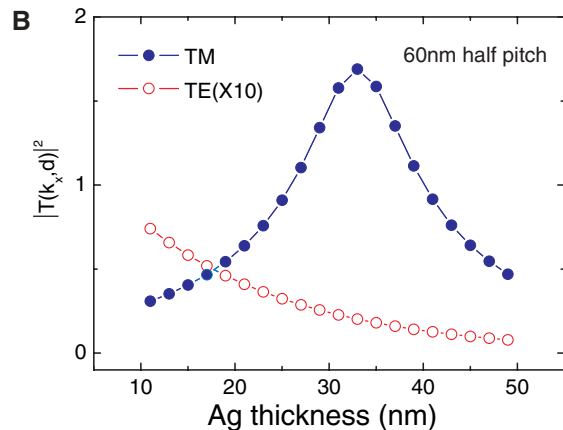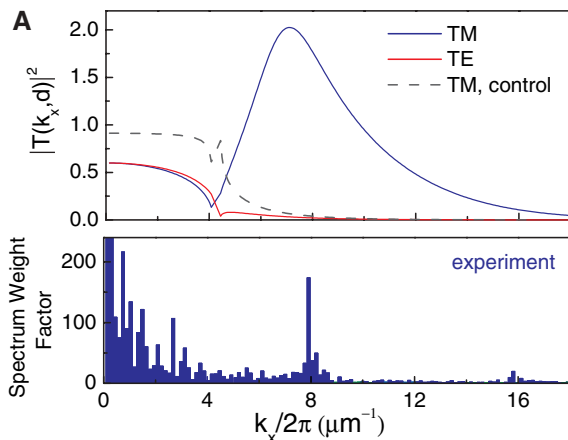
For enhanced transmission of evanescent waves (23), it is found that an asymptotic impedance match ($k_{zi}/\varepsilon_i + k_{zj}/\varepsilon_j = 0$) has to be met at the surface of the silver, known as the surface plasmon excitation condition (k_{zi}, cross-plane wave vector in silver; ε_i, permittivity of silver; k_{zj}, cross-plane wave vector in dialectric; and ε_j, permittivity of dialectric). It is widely known in metal optics that when the two media take the opposite sign in permittivity and $|\varepsilon_i| >> \varepsilon_j$, only surface plasmons at the narrow range of in-plane wave vector (k_x) that are close to k_0 can be resonantly coupled. However, less well known is that when $|\varepsilon_i| \sim \varepsilon_j$ and they are of opposite sign, the excitable surface plasmon band of k_x is significantly broadened, resulting in the superlensing effect (1).

Figure 1 shows a set of objects inscribed onto a chrome screen. The objects, placed about 40 nm away from the 35-nm silver film, are imaged onto the photoresist on the other side of the silver film under ultraviolet (UV) illumination (at a wavelength of 365 nm). Using focused ion beam (FIB) lithography, the chrome objects are patterned on quartz and then planarized, using a 40-nm-thick layer of polymethyl methacrylate (PMMA). The chrome masks are approximated as a binary object because in the

UV, chromium (permittivity = –8.55 + i8.96) is away from the plasmon resonance and possesses low skin depth (~15 nm) (24). Subsequently, a 35-nm-thick layer of silver, the superlens, is evaporated over the PMMA spacer layer, followed by coating with a 120-nm-thick negative photoresist [NFR105G, Japan Synthetic Rubber Microelectronics (JSR Micro)] to record the near-field image. The substrate is then flood-exposed under an I-line (365-nm) mercury lamp (25). The exposure flux is 8 mW/cm², and an optimal exposure time of 60 s is applied. It is essential to reduce the surface root mean square modulation below 1 nm for both the silver and PMMA surfaces (Fig. 2E); otherwise, the dispersion characteristics of the superlens would be modified and would in turn smear the details of the recorded image (19). The optical image is converted into topographic modulations by developing the negative photoresist and is mapped using atomic force microscopy (AFM). The image of an array of 60-nm-wide nanowires on a 120-nm pitch is shown in Fig. 2A. The Fourier-transformed spectrum shows a sharp peak, corresponding to a pitch of 126 ± 7 nm (Fig. 3A, bottom panel). With careful control

Fig. 3. The computed transfer function of the superlens system (the square modulus of the image, *E*-field normalized by object *E* field in wave vector space) (*27*). (**A**) (Top) Blue and red solid curves show the overall transmission of TM and TE waves over the combination of a 40-nm PMMA spacer layer and a 35-nm silver film, respectively; the black dashed curve is calculated by replacing the 35-nm silver layer with a 35-nm PMMA layer (TM polarization) in the control experiment. The abscissa is the normalized lateral wave vector. *T*, transmission coefficient; *d*, thickness of silver. (Bottom) The navy columns show the experimentally resolved spectral components of the imaged object. The major peak indicates a 63 ± 4 nm half-pitch. (**B**) The image transfer function for TM and TE fields versus silver thickness for 60-nm half-pitch objects.
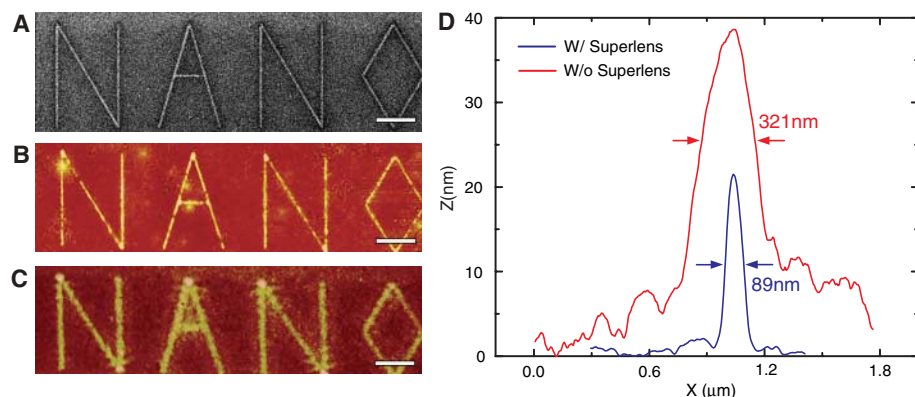
Fig. 4. An arbitrary object "NANO" was imaged by silver superlens. (**A**) FIB image of the object. The linewidth of the "NANO" object was 40 nm. Scale bar in (A) to (C), 2 μm. (**B**) AFM of the developed image on photoresist with a silver superlens. (**C**) AFM of the developed image on photoresist when the 35-nm-thick layer of silver was replaced by PMMA spacer as a control experiment. (**D**) The averaged cross section of letter "A" shows an exposed line width of 89 nm (blue line), whereas in the control experiment, we measured a diffraction-limited full width at half-maximum line width of 321 ± 10 nm (red line).

of the surface morphology of the PMMA and silver surface, we recorded the photoresist images with typical average height modulations of 5 to 10 nm (Fig. 2C). The result indicates sub–diffraction-limited imaging with half-pitch resolution down to 60 nm, or $\lambda/6$, using a silver superlens. The control experiments in which the silver film is replaced by 35-nm-thick PMMA show no evidence of imaging contrast from the subwavelength object, regardless of the optimization of imaging processes (Fig. 2, B and D). Our observation is further verified by a simple analysis of the evanescent decay of these subwavelength features. For a line-array object of period *a*, the intensity of evanescent waves decays with a characteristic length *Z*, given by $Z^{-1} = 4\pi\sqrt{a^{-2} - \varepsilon\lambda^{-2}}$ (*26*). With the permittivity of the surrounding media $\varepsilon \sim 2.4$, a decay length of 11 nm is estimated for the 60-nm half-pitch. Without a superlens to enhance and transmit evanescent waves, it is difficult to resolve a 60-nm half-pitch object from a distance of 75 nm away, as we observed in the control experiments.

For the perfect lens originally proposed by Pendry, the entire Fourier spectrum of the image should be transferred uniformly without loss or distortion. However, a slab lens made of real materials with dispersive negative permittivity (such as silver) or permeability inevitably has losses and only asymptotically approaches a perfect lens at the quasi-static limit. Yet, such a lens system greatly enhances the essential portion of the evanescent spectrum, allowing subwavelength imaging resolution. We term such system a superlens, in comparison to an ideally perfect lens. Superlensing requires rather stringent conditions to maximize the enhancement over a broad band of evanescent waves. It is crucial to find a wavelength range where the wavelength-dependent permittivity of silver is nearly equal to and opposite that of the adjacent medium, which is the PMMA spacer and photoresist in this experiment. The

resolving power of this system can be measured by the optical transfer function, defined as the ratio of image field to object field, $|E|_{\text{img}}/|E|_{\text{obj}}$, with given lateral wave vector k_x. Using the Fresnel formula of a stratified medium (*18*), we computed the optical transfer function of a silver superlens system, taking into consideration the absorption in silver and in the adjacent media (Fig. 3). From Fig. 3A, we estimate that a range of evanescent components from 2 to 4 k_0 can be efficiently enhanced and recovered by surface plasmon excitations, which is much broader than the conventional narrow resonance (typically <10% of k_0). The calculation shows that the slight absorptions from PMMA and the photoresist have only negligible effects on the imaging quality.

Although the illumination is normal to the plane of the object, the subwavelength object scatters the incident radiation in different directions. Two types of polarization for the scattered waves in reference to the plane of the silver superlens are classified: (i) waves with a magnetic field component parallel to the plane have TM polarization, and (ii) waves with an electric field parallel to the plane have transverse electric (TE) polarization. Whereas a broad band of TM evanescent waves are resonantly coupled over the 35-nm silver superlens to form a sub–diffraction-limited image, the TE fields are significantly damped out (Fig. 3A), which is consistent with theoretical estimations of the image resolution calculated against the loss of natural silver (*18*, *19*). Even though the PMMA and the photoresist slightly detune the surface plasmon resonance at the interfaces, the finite thickness of the silver slab ensures that they will be excited (*22*), allowing enhanced transfer of a broad evanescent spectrum. Because the 60-nm half-pitch object carries fundamental wave vectors that fall within the broad band of enhancement by the superlens (Fig. 3A, top panel), the corresponding spectrum peak is clearly observed in the recorded image, as seen in our experiment (Fig. 3A, bottom panel). In

Fig. 3B, we calculated the transfer function of the 60-nm half-pitch object for various silver film thicknesses. Assisted by surface plasmon excitation, a maximum enhancement of the selected subwavelength feature was reached for a 35-nm-thick silver slab. Above a thickness of 40 nm, the enhancement was damped by material absorption, destroying the superlensing effect. Such a critical thickness gives a measure for the efficient coupling of the evanescent modes at two interfaces of the silver film. The existence of this critical thickness is in good agreement with our previous finding (15).

The silver superlens can also image arbitrary nanostructures with sub–diffraction-limited resolution (Fig. 4). The recorded image "NANO" in Fig. 4B shows that we can faithfully reproduce the fine features from the mask (Fig. 4A) in all directions with good fidelity. As previously discussed, only the scattered TM evanescent waves from the object are coupled into the surface plasmon resonance of the silver film, and they become a primary component for restoring a sub–diffraction-limited image. For comparison, Fig. 4C displays the control experiment performed on the same mask, with "NANO" embedded in 75-nm planarized PMMA. With the same exposure condition, we observed the image of "NANO" with much wider lines, even with the extended development time (>1 min). Because the lines are a few micrometers apart, the subwavelength openings can be treated as isolated line sources, with a broad band of Fourier spectrum: The larger Fourier components decay strongly, and only the smaller Fourier components reach the imaging plane, resulting in a diffraction-limited image as shown in Fig. 4C.

In contrast, with a silver superlens, we can resolve an average line width of 89 nm (Fig. 4D), which is much smaller than that of the diffraction-limited image. With natural and structured plasmons (28–31) in metals and phonon polaritons in semiconductors, a potential low-loss, high-resolution superlens is achievable.

References and Notes

1. J. B. Pendry, *Phys. Rev. Lett.* **85**, 3966 (2000).
2. H. I. Smith, *Proc. IEEE* **62**, 1361 (1974).
3. U. Ch. Fischer, H. P. Zingsheim, *J. Vac. Sci. Technol.* **19**, 881 (1981).
4. J. G. Goodberlet, H. Kavak, *Appl. Phys. Lett.* **81**, 1315 (2002).
5. X. Luo, T. Ishihara, *Appl. Phys. Lett.* **84**, 4780 (2004).
6. M. C. K. Wiltshire *et al.*, *Science* **291**, 849 (2001).
7. M. C. K. Wiltshire *et al.*, *Opt. Express* **11**, 709 (2003).
8. R. A. Shelby, D. R. Smith, S. Schultz, *Science* **292**, 77 (2001).
9. A. K. Iyer, P. C. Kremer, G. V. Eleftheriades, *Opt. Express* **11**, 696 (2003).
10. A. Grbic, G. V. Eleftheriades, *Phys. Rev. Lett.* **92**, 117403 (2004).
11. T.-J. Yen *et al.*, *Science* **303**, 1494 (2004).
12. S. Linden *et al.*, *Science* **306**, 3531 (2004).
13. C. G. Parazzoli *et al.*, *Phys. Rev. Lett.* **90**, 107401 (2003).
14. A. A. Houck, J. B. Brock, I. L. Chuang, *Phys. Rev. Lett.* **90**, 137401 (2003).
15. D. R. Smith, J. B. Pendry, M. C. K. Wiltshire, *Science* **305**, 788 (2004).
16. P. V. Parimi, W. T. Lu, P. Vodo, S. Sridhar, *Nature* **426**, 404 (2003).
17. Z. Liu, N. Fang, T.-J. Yen, X. Zhang, *Appl. Phys. Lett.* **83**, 5184 (2003).
18. N. Fang, X. Zhang, *Appl. Phys. Lett.* **82**, 161 (2003).
19. D. R. Smith *et al.*, *Appl. Phys. Lett.* **82**, 1506 (2003).
20. D. O. S. Melville, R. J. Blaikie, *J. Vac. Sci. Technol.* **B22**, 3470 (2004).
21. D. O. S. Melville, R. J. Blaikie, *J. Opt.* **A7**, S176 (2005).
22. S. A. Ramakrishna, D. Schurig, D. R. Smith, S. Schultz, J. B. Pendry, *J. Mod. Opt.* **49**, 1747 (2002).
23. N. Fang, Z. Liu, T.-J. Yen, X. Zhang, *Opt. Express* **11**, 682 (2003).
24. In our estimation, an ideal mask was assumed to have perfect binary near-field profiles, but the actual intensity may be influenced by the material and geometries of the subwavelength mask near the superlens. Thus, Fig. 3 should be regarded as a general guideline to the performance of the real system. A more accurate description can be given by full vector electromagnetic simulations of the system, such as in (21).
25. The image-recording conditions have been optimized to obtain the best possible image contrast in all experiments in this report. See the details of the control experiment in the supporting material on *Science* Online.
26. E. Loewen, E. Popov, *Diffraction Gratings and Applications* (Marcel Dekker, New York, 1997).
27. To compute the image transfer function presented in Fig. 3, the dielectric constant (2.3013 + 0.0014i) of PMMA is taken from the 495PMMA product datasheet (Microchem), the refractive index (n = 1.6099) of NFR105G is taken from JSR Micro, and a typical value of κ = 0.003 is taken into account for the absorption of the photoresist. In the computation, we assume that the photoresist occupies the top half of the space, whereas experimentally the actual photoresist layer thickness is 120 nm. The permittivity of silver (−2.4012 + 0.2488i) is taken from (32).
28. J. B. Pendry, A. J. Holden, W. J. Stewart, I. Youngs, *Phys. Rev. Lett.* **76**, 4773 (1996).
29. H. J. Lezec *et al.*, *Science* **297**, 820 (2002).
30. T. W. Ebbesen, H. J. Lezec, H. F. Ghaemi, T. Thio, P. A. Wolff, *Nature* **391**, 667 (1998).
31. J. B. Pendry, L. Martín-Moreno, F. J. Garcia-Vidal, *Science* **305**, 847 (2004).
32. P. B. Johnson, R. W. Christy, *Phys. Rev. B* **6**, 4370 (1972).
33. The authors acknowledge support from the Office of Naval Research (ONR)/Defense Advanced Research Projects Agency Multidisciplinary University Research Initiative (MURI) (ONR grant N00014-01-1-0803) and from NSF for the Center for Nanoscale Science and Engineering (grant DMI-0327077).

Monodisperse Double Emulsions Generated from a Microcapillary Device

A. S. Utada,[1] E. Lorenceau,[1] D. R. Link,[1,2] P. D. Kaplan,[3] H. A. Stone,[1] D. A. Weitz[1,2]

Double emulsions are highly structured fluids consisting of emulsion drops that contain smaller droplets inside. Although double emulsions are potentially of commercial value, traditional fabrication by means of two emulsification steps leads to very ill-controlled structuring. Using a microcapillary device, we fabricated double emulsions that contained a single internal droplet in a core-shell geometry. We show that the droplet size can be quantitatively predicted from the flow profiles of the fluids. The double emulsions were used to generate encapsulation structures by manipulating the properties of the fluid that makes up the shell. The high degree of control afforded by this method and the completely separate fluid streams make this a flexible and promising technique.

Mixing two immiscible fluids produces an emulsion, which is defined as a dispersion of droplets of one fluid in a second fluid. Although they are not in equilibrium, emulsions can be metastable, with the droplets retaining their integrity for extended periods of time if their interface is stabilized by a surfactant. Emulsions play critical roles in many forms of processing and in coatings, foods, and cosmetics (1). One common use is to compartmentalize one fluid in a second, which is particularly important for packaging and stabilizing fluids and other active ingredients. Even more control and flexibility for encapsulation can be achieved through the use of double emulsions, which are emulsions with smaller droplets of a third fluid within the larger drops. The intermediate fluid adds an additional barrier that separates the innermost fluid from the outer fluid, or the continuous phase. This makes double emulsions highly desirable for applications in controlled release of substances (2–4); separation (5); and encapsulation of nutrients and flavors for food additives (6–8); and for the control of encapsulation, release, and rheology for personal care products (4, 9–11). Additional flexibility is achieved by controlling the state of the

[1]Division of Engineering and Applied Sciences, [2]Department of Physics, Harvard University, Cambridge, MA 02138, USA. [3]Unilever Skin Global Innovation Center, 40 Merritt Boulevard, Trumbull, CT 06611, USA.